Science of the Total Environment 729 (2020) 138892

Contents lists available at ScienceDirect

Science of the Total Environment

journal homepage: www.elsevier.com/locate/scitotenv

Phosphorus recovery by core-shell γ-Al_2O_3/Fe_3O_4 biochar composite from aqueous phosphate solutions

Qingliang Cui [a,b,c], Jinling Xu [d], Wei Wang [e], Lianshuai Tan [a], Yongxing Cui [b,c], Tongtong Wang [a], Gaoliang Li [b,c], Diao She [a,b], Jiyong Zheng [a,b,*]

[a] State Key Laboratory of Soil Erosion and Dryland Farming on Loess Plateau, Northwest A&F University, Yangling 712100, PR China
[b] State Key Laboratory of Soil Erosion and Dryland Farming on Loess Plateau, Institute of Soil and Water Conservation, Chinese Academy of Sciences and Ministry of Water Resources, Yangling, Shaanxi 712100, China
[c] University of Chinese Academy of Sciences, Beijing 100049, PR China
[d] College of Geography and Environment, Shandong Normal University, Jinan, Shandong 250014, PR China
[e] Ningxia Agricultural Development Center, Yinchuan, Ningxia 750000, PR China

HIGHLIGHTS

- Dual-modification was designed to prepare core-shell γ-Al_2O_3/Fe_3O_4 biochar (AFBC).
- AFBC with excellent capacity and stability has no pollution during P recovery.
- Electrostatic attraction and inner-sphere complexation were the main mechanisms.
- Inner-sphere P complexes were monodentate and bidentate species.
- After 5 reusable experiment, removal and desorption efficiency higher than 91.0%

GRAPHICAL ABSTRACT

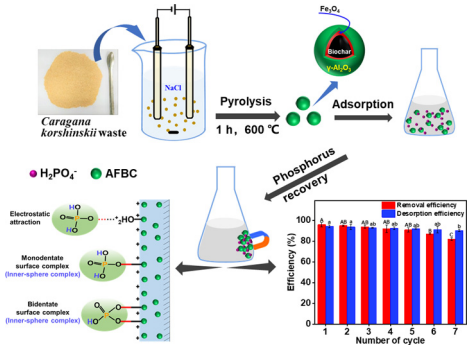

ARTICLE INFO

Article history:
Received 25 November 2019
Received in revised form 12 April 2020
Accepted 20 April 2020
Available online 24 April 2020

Guest Editor: Pengfei Sun

Keywords:
Phosphorus recovery
γ-Al_2O_3/Fe_3O_4 biochar
Core-shell structure
Adsorption mechanisms
Reusability

ABSTRACT

Biochar can act as an adsorbent for phosphate removal from water sources, which can be highly beneficial in limiting eutrophication and recycling elemental phosphorus (P). However, it is difficult to use a single biochar material to overcome problems such as low adsorption efficiency, difficulty in reuse, and secondary pollution. This study addresses these challenges using a novel core-shell structure γ-Al_2O_3/Fe_3O_4 biochar adsorbent (AFBC) with significant P uptake capabilities in terms of its high adsorption capacity (205.7 mg g^{-1}), magnetic properties (saturation magnetization 24.70 emu g^{-1}), and high reuse stability (91.0% removal efficiency after five adsorption-desorption cycles). The highest partition coefficient 1.04 mg g^{-1} μM^{-1}, was obtained at a concentration of 322.89 μM. Furthermore, AFBC exhibited strong regeneration ability in multiple cycle trials, making it extremely viable for sustainable resource management. P removal mechanisms, i.e., electrostatic attraction and inner-sphere complexation, were explained using Fourier transform infrared (FT-IR) spectra and X-ray photoelectron spectroscopy (XPS) measurements. A surface complexation model was established by considering the formation of monodentate mononuclear and bidentate binuclear surface complexes of P to illustrate the adsorption process. Owing to its high adsorption efficiency, easy separation from water, and environmental friendliness, AFBC is a potential adsorbent for P recovery from polluted waters.

* Corresponding author at: State Key Laboratory of Soil Erosion and Dryland Farming on Loess Plateau, Northwest A&F University, Yangling 712100, PR China.
E-mail address: zhjy@ms.iswc.ac.cn (J. Zheng).

https://doi.org/10.1016/j.scitotenv.2020.138892
0048-9697/

1. Introduction

Phosphorus (P), an essential nutrient for all life, plays a critical and irreplaceable role in our environment. However, overutilization of P in the environment for meeting the needs of the Green Revolution as well as industrial requirements has resulted in frequent eutrophication of water bodies and a significant threat to human health (Mayer et al., 2016; Schmale et al., 2019; Tonini et al., 2019; Vilmin et al., 2018; Wu et al., 2011). Moreover, P is a nonrenewable resource and depletion in its global supply is predicted in ~200 years based on the current rate of consumption (Huang et al., 2014). Therefore, it is crucial to develop new technologies for P removal and recovery from P-polluted surface waters to reduce the damage to aquatic environments and ensure sustainable management of this critical resource.

Biochar is recognized as a promising platform material for the synthesis of a variety of functional materials and has been widely studied as a carrier for stable metal nanoparticles (Liu et al., 2015; Xiao et al., 2018; Yang et al., 2019a). Tremendous effort has been directed toward designing high-performance anion adsorption biochar materials tailored for P uptake applications. However, the combined features of high P adsorption capacity, an acceptable lack of secondary pollution, effective adsorption selectivity, and high reuse stability have rarely been integrated into a single material. For instance, the surface of biochar has been modified with calcium and magnesium to improve biochar P adsorption performance (Kong et al., 2018; Li et al., 2018; Pinto et al., 2019; Wang et al., 2018; Yi and Chen, 2018), however, P recovery from solution is challenging due to the small adsorbent particle size. Biochar materials modified with iron have strong phosphate removal abilities as well as magnetic properties, making biochar collection in solution feasible (Cai et al., 2017; Chen et al., 2011; Tang et al., 2017; Wang et al., 2019; Zhu et al., 2018). Despite this, iron exposed on the biochar surface can easily enter the solution and cause secondary pollution. Thus, the need to improve the practicality and stability of synthetic materials warrants further in-depth investigation. In recent years, chemical reagents have been used to synthesize compounds for phosphate removal from solution (Shemer et al., 2019; Yan et al., 2016; Yang et al., 2019b). These compounds, without biochar as a carrier, tend to accumulate densely which limits their removal effectiveness.

In addition, core-shell composite materials have received extensive attention in the field of environmental pollution (Han et al., 2019; Jung et al., 2019; Lan et al., 2013). These materials make full use of the special characteristics of the nuclear structure carrier, namely the oxygen-containing functional groups and pores, while protecting the unstable compound parts, such as shell structure. Therefore, this study takes full advantage of the core-shell structure to synthesize a composite biochar with a double core-shell structure. The synthesis method adopts a two-step electrical assistant method, which is an improvement over the electrical modification method proposed by Jung et al. (2015, 2017a). The improved method can generate a double shell structure. The inner shell structure is magnetic iron (II, III) oxide (Fe_3O_4), whereas the outer shell structure is aluminum oxide (γ-Al_2O_3), a porous material with a strong adsorption capacity often used as a composite shell structure (Lan et al., 2013; Li et al., 2014). As an outer shell structure, it can encase the inner shell structure and also efficiently absorb phosphate in solution.

The precursor of biochar is *Caragana korshinskii* (*C. korshinskii*), a perennial shrub, which is underutilized in the arid and semi-arid areas of China. Due to the aforementioned biochar issues, a core-shell structure γ-Al_2O_3/Fe_3O_4 *C. korshinskii* biochar composite (AFBC) was produced. This novel composite could provide a carrier for shell structure, whereas γ-Al_2O_3 and Fe_3O_4 particles could improve biochar adsorption performance by providing new binding sites for phosphate along with possessing reliable separation properties. Thus, this study aims to: (i) synthesize AFBC and characterize its structure and morphology, (ii) investigate the characteristics and underlying mechanisms of P adsorption by AFBC, and (iii) determine the reuse stability of P recovery by AFBC. The findings could be of great technical value to facilitate the development and implementation of new magnetic biochar materials for P remediation and recovery from the environment.

2. Materials and methods

2.1. Materials and chemicals

The *C. korshinskii* employed in this study was acquired from Guyuan, Ningxia Hui Autonomous Region, China. All chemical reagents (including NaH_2PO_4, NaOH, and HCl etc.) were analytically pure and were provided by Sinopharm Chemical Reagent Co., Ltd. (Shanghai, China). Iron and aluminum electrodes were provided by Goodfellow Cambridge Ltd. (UK). All chemical reagents were prepared using deionized (DI) water.

2.2. AFBC synthesis

Preparation of AFBC used *C. korshinskii* as the raw organic material and iron and aluminum as electrodes (each electrode had dimensions of Φ 10 mm × 150 mm, effective surface area 75.6 cm^2); pyrolysis via two-step electro-assisted modification was performed. *C. korshinskii* powder (particle size 0.15 mm, sieved) was immersed into 500 mL of a 1.0 g L^{-1} NaCl solution. Both the cathode and anode were iron electrodes. For electro-modification, a current density (123.91 mA cm^{-2}) was applied for 15 min using a power supply (FTS12–100, Faithtech Co., China). After aging for 30 min, sediments were collected using magnets, washed three times with DI water, and dried in an atmosphere of N_2 at 60 °C. Then, the obtained Fe_3O_4 magnetic biomass was once again immersed in 500 mL of a 1.0 g L^{-1} NaCl solution, after which the iron electrodes were replaced with aluminum electrodes and electrified for an additional 15 min. After aging for 30 min, sediments were again collected using a magnet, washed three times with DI water, and dried in an atmosphere of N_2 at 60 °C. Then, the dried sediments were placed in a muffle furnace for pyrolysis to obtain AFBC (600 °C, 1 h, under a constant N_2 flow). Simultaneously, some of the raw organic material and the obtained Fe_3O_4 magnetic biomass were pyrolyzed into raw biochar (BC) and Fe_3O_4 biochar (FBC) using the same pyrolysis method. The resulting pyrolyzed BC, FBC, and AFBC were ground to a powder and screened to a particle size <0.15 mm.

2.3. Characterization

Samples were analyzed by X-ray diffraction (XRD) using a computer-controlled X-ray diffractometer (XRD-6100, Shimadzu) to determine the crystalline structure. Fourier transform infrared (FT-IR) spectra within a wavenumber range of 400–4000 cm^{-1} allowed study of AFBC surface functionality (NICOLET iS50, Thermo Scientific). A scanning electron microscope (FE-SEM, JEOL 7800F) was employed to visualize the surface morphology and structure of the modified biochar, and the elemental mapping of surface material was carried out via electron dispersive X-ray spectrometer (EDS) analysis. Zeta potential was measured using a Zetasizer Nano ZSE (Malvern, England). X-ray photoelectron spectroscopy (XPS) (ESCALab Xi+, Thermo Scientific) was used to determine the surface elemental composition of the samples. The magnetic hysteresis loops of samples were measured by a vibrating sample magnetometer (VSM; MPMS-SQUID-094, Quantum Design) at 25 °C between −10 and 10 kOe. Specific surface areas and total pore volumes were calculated by N_2 adsorption/desorption isotherms at −196 °C using a Micromeritics ASAP 2020 Plus HD88 analyzer. Aluminum and iron ions were determined via inductively coupled plasma-mass spectrometry (ICP-MS; NexION 350D, PerkinElmer).

2.4. Adsorption experiments

An initial stock solution of P (1000 mg L^{-1}) was prepared using NaH_2PO_4 and diluted at the various phosphate concentrations (10, 35, 50, 90, 120, 160, 200, 300, 400, and 500 mg L^{-1}). All the adsorption experiments were performed in 150-mL conical flasks filled with 50 mL of 50 mg L^{-1} phosphate solution with an original pH of 5.0 and 0.05 g of AFBC. Conical flasks were then placed in a thermostatic oscillator for 12 h at 120 rpm and 25 °C. Thereafter, the samples were immediately separated with a 0.45 μm membrane filter. Factors such as the pH (3.0–11.0), contact time ($0-12h$), and P concentration (5–500 mg L^{-1}) were varied to optimize the adsorption process and obtain phosphate adsorption kinetic and isotherm data. The initial pH of solutions was adjusted using 0.1 mol L^{-1} HCl or 0.1 mol L^{-1} NaOH. The experimental results were analyzed using three kinetic models (pseudo-first-order, pseudo-second-order, and intraparticle diffusion) and three isotherm models (Langmuir, Freundlich, and Langmuir-Freundlich). Table S1 shows the expressions of the employed models. The remaining P concentrations were determined by the molybdenum blue spectrophotometric method (Murphy and Riley, 1962) at 880 nm with a UV-2600 spectrophotometer (Shimadzu, Japan). The amount of phosphate adsorbed by the AFBC, in addition to its removal efficiency (%), were calculated using Eqs. (1) and (2):

$$q_e = \frac{(C_i - C_e)}{m} \times V \quad (1)$$

$$\text{Removal}(\%) = \frac{(C_i - C_e)}{C_i} \times 100 \quad (2)$$

where C_i and C_e (mg L^{-1}) refer to the P concentration initially and at equilibrium, respectively, q_e (mg g^{-1}) is the equilibrium adsorption capacity of AFBC for adsorbate, m (g) is the AFBC mass, and V (L) is the solution volume.

To investigate the selectivity of AFBC for phosphate uptake, competitive adsorption experiments were conducted through the addition of common coexisting anions, such as sulfate, chloride, bicarbonate, nitrate, fluoride, and their mixture, into the phosphate solutions at different concentrations (0, 0.1, and 1.0 mmol L^{-1}). To determine whether any dissolution of Fe and Al occurred from AFBC, the AFBC was immersed in DI water at pH 5.0 and 10.0 for 12 h.

2.5. Reusability study

To evaluate the reusability of the AFBC, seven adsorption-desorption cycles were carried out. First, a phosphate adsorption test was carried out with an initial P concentration of 35 mg L^{-1}. Then, the saturated AFBC was collected immediately from the solution via an ordinary magnet after reaching the equilibrium stage. The collected AFBC was immersed in solutions with different NaOH concentrations (1.0×10^{-6}, 1.0×10^{-5}, 1.0×10^{-4}, 1.0×10^{-3}, and 1.0×10^{-2} mol L^{-1}). After determining suitable desorption conditions, the recyclability following seven cycles was tested, and the amount of adsorbed phosphate and removal efficiency were determined using Eqs. (1) and (2). Desorbed P concentrations were measured as described earlier, and the desorption efficiency (%) was calculated using Eq. (3):

$$\text{Desorption}(\%) = \frac{C_d \times V_d}{(C_i - C_e) \times V} \times 100 \quad (3)$$

where C_d (mg L^{-1}) is the concentration of P in the desorbed solution, and V_d (L) is the solution volume. All experiments were conducted in triplicate; additional measurements were conducted when the difference between duplicates was >5%.

2.6. Statistical analysis

A one-way ANOVA was used to examine the effects of numbers of adsorption-desorption cycles on adsorption and desorption efficiency; then, mean comparisons were performed using Tukey's multiple comparisons test ($P < .05$).

3. Results and discussion

3.1. General characteristics of AFBC

Table 1 shows the physicochemical properties of BC, FBC, and AFBC. The carbon (C) contents of BC, FBC, and AFBC were 68.43, 54.52, and 39.44 wt%, respectively. The oxygen (O) content in the BC, FBC, and AFBC were 31.57, 34.47, and 38.18 wt%, respectively. The iron (Fe) contents in FBC and AFBC were 11.01 and 7.03 wt%, respectively. The aluminum (Al) content in AFBC was 15.35 wt%. The N_2 adsorption-desorption isotherm and pore size distribution of BC, FBC, and AFBC are shown in Fig. S1. The specific surface areas of BC, FBC, and AFBC were 133.49, 89.37, and 233.29 m^2 g^{-1}, respectively. The total pore volumes of the BC, FBC, and AFBC were 0.09, 0.05, and 0.13 cm^3 g^{-1}, respectively. Compared with BC, the O content of FBC increased after introduction of Fe_3O_4. Conversely, the C content, specific surface area, and total pore volume decreased. This was attributed to Fe_3O_4 filling the biochar pores. Compared with BC, the C content of AFBC decreased after the introduction of γ-Al_2O_3 and Fe_3O_4. Conversely, the O content increased, as did specific surface area and total pore volume. This was due to the large specific surface area and total pore volume of the γ-Al_2O_3 incorporated into the AFBC. The XRD patterns of AFBC within a 10–80° range are presented in Fig. 1a. The diffraction peaks at 2θ positions 30.1°, 35.5°, 43.1°, 56.9°, 62.5°, and 74.1° matched well with the (220), (311), (400), (511), (440), and (533) lattice planes, and the positions of the diffraction peaks were consistent with the standard card of Fe_3O_4 (JCPDS No. 19–0629). Although these peaks matched the standard card of Fe_3O_4, they also matched well with the standard card of γ-Fe_2O_3 (JCPDS No.25–140; Du et al., 2020). The generation of Fe_3O_4 will be proved in the FT-IR and XPS sections. The diffraction peaks at 2θ positions 19.63°, 31.9°, 37.8°, 46.2°, and 66.4° matched well with the (111), (220), (110), (202), and (214) lattice planes, and the positions of the diffraction peaks were consistent with the standard card of γ-Al_2O_3 (JCPDS No. 50-1684). The narrow, strong diffraction peaks indicated that γ-Al_2O_3 had highly crystalline structures. The sharpness and intensity of the peaks indicated that the AFBC had a highly crystalline structure. This also indicated simultaneous γ-Al_2O_3 generation in the modified samples.

The FT-IR spectra of AFBC both before and after adsorbing phosphate are presented in Fig. 1b. Table S3 summarizes the peak parameters deduced from FT-IR spectra of AFBC before and after P adsorption. Peaks at approximately 2920–2925 cm^{-1} corresponded to C—H vibration, while peaks at approximately 1021 cm^{-1} were attributed to C—O vibration. The benzene ring C═C stretching peak at 1458 cm^{-1} implies that the aromatization process happened during the biochar preparation (Leng et al., 2015). Such characteristic peaks confirmed that AFBC presented a biochar-like structure. An –OH stretching and bending vibration was observed at 3435 and 1634 cm^{-1}, respectively, suggesting hydrogen bonding between water and the composite. The peak locating

Table 1
Physiochemical properties of materials.

Material	C (wt %)	O (wt %)	Fe (wt %)	Al (wt %)	Surface area (m^2 g^{-1})	Total pore volume (cm^3 g^{-1})	Saturated magnetization (emu g^{-1})
BC	68.43	31.57	–	–	133.49	0.09	–
FBC	54.52	34.47	11.01	–	89.37	0.05	35.80
AFBC	39.44	38.18	7.03	15.35	233.29	0.13	24.70

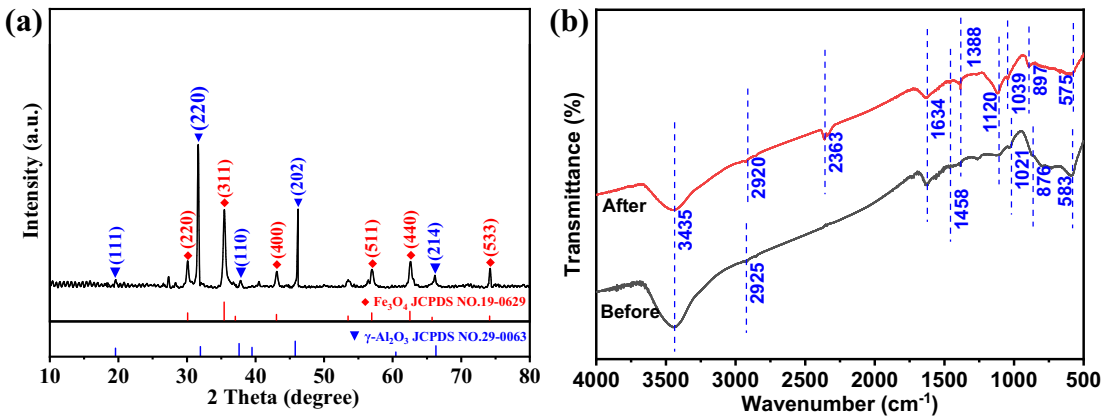

Fig. 1. (a) XRD pattern of AFBC and (b) FT-IR spectra for AFBC before and after phosphate adsorption.

at ~1388 cm^{-1} belonged to a C–H/C=O stretching vibration (Yang et al., 2019c). The strong peak at 583 cm^{-1} was attributed to the Fe—O lattice vibration of Fe_3O_4 (Yan et al., 2015), indicating the existence of Fe_3O_4 particles. Compared with the peak at 583 cm^{-1} prior to P adsorption, the strength of the Fe—O lattice vibration peaked at 575 cm^{-1} after phosphate adsorption. However, the Fe—O group could still be easily observed, suggesting that the Fe—O group also contributed to the adsorption of P ions. The strong peak at 876 cm^{-1} was attributed to the Al—O lattice vibration of Al_2O_3, while the characteristic peak at 897 cm^{-1} was attributed to the stretching and bending mode of Al—O (Lǔ et al., 2013; Li et al., 2016). For the phosphate-adsorbed sample, the characteristic peaks at 1120 and 1039 cm^{-1} were interpreted as the combined spectrum band of P—O stretching and bending vibrations, respectively, demonstrating the incorporation of the P-containing acid root into the adsorbed sample (Li et al., 2018; Salama, 2018). Peaks at 1120 and 1039 cm^{-1} appear to characterize monodentate mononuclear and bidentate binuclear surface complexes of P, respectively (Xu et al., 2019). The peak located at ~2363 cm^{-1} belongs to the $H_2PO_4^-$ group. Therefore, FT-IR analysis verified the presence of Al_2O_3 and Fe_3O_4 components in the synthesized AFBC, and confirmed successful P capture by detecting correlation vibrational bands.

Magnetization properties of AFBC are summarized in Fig. S2, and were determined by magnetization response testing at 25 °C. Magnetic remanence (*Mr*) of AFBC was almost zero, and specific magnetic saturation was 24.70 emu g^{-1}. The small *Mr* value indicates that AFBC exhibited superparamagnetic behavior, which facilitates AFBC separation from the treated solution by a permanent magnet (Fig. S2).

The chemical composition and electronic state of the constituent elements in the AFBC were further evaluated via XPS. The usual peaks of Fe 2p (711.0 eV), Al 2p (74.5 eV), C 1s (284.1 eV), and O 1s (531.8 eV) present in the AFBC (Fig. 2a) illustrated the coexistence of Fe, Al, and O, which additionally supported the successful preparation of Fe_3O_4 and γ-Al_2O_3 nanocomposites. Furthermore, a P 2p peak was clearly observed after phosphate adsorption at 133.6 eV, indicating that AFBC successfully adsorbs phosphate. In the Fe 2p spectrum (Fig. 2b), previous studies have found that the binding energy of Fe $2p_{3/2}$ is at 711.2 eV and Fe $2p_{1/2}$ is at 724.6 eV (Lu et al., 2005). The Fe $2p_{3/2}$ peak at 710.8 eV (Fe(II)) and 713.6 eV (Fe(III)), and Fe $2p_{1/2}$ peak at 723.7 eV (Fe(II)) and 725.1 eV (Fe(III)), both of which are present in Fe_3O_4. (Shanmugam et al., 2009; Zhu et al., 2019). The absence of a satellite peak at ~719.0 eV, a characteristic of Fe_2O_3, was indicative of the formation of a Fe_3O_4 phase in the AFBC, which was consistent with the XRD results.

SEM images were used to investigate the morphology and structural features of BC (Fig. S3a), FBC (Fig. S3b), and AFBC (Fig. S3c). The surface of the BC was columnar and smooth with some irregular cracks and pores. However, some small particles and flocculent materials appeared onto the surface of FBC and AFBC that can be considered as Fe_3O_4 and γ-Al_2O_3, respectively, after electro-assisted modification compared with BC. To confirm the presence of Fe_3O_4 and γ-Al_2O_3 on the biochar surface, elemental mapping of these composites was conducted (Fig. S3). EDS elemental mapping revealed the Fe distribution on the inner shell structure surface (FBC surface) and C, O, Fe, and Al distributions over the mapped AFBC surface region. This indicates that Fe is dispersed in FBC and AFBC. Table S2 summarizes the ion dissolution concentration of FBC and AFBC. With an increase in the dissolution time, the concentrations of Al^{3+} and Fe^{2+}/Fe^{3+} of FBC and AFBC increased, and the Fe^{2+}/Fe^{3+} concentration of FBC was higher than that of AFBC. This indicates that Fe_3O_4 is highly protected by the shell structure of γ-Al_2O_3. Thus, it

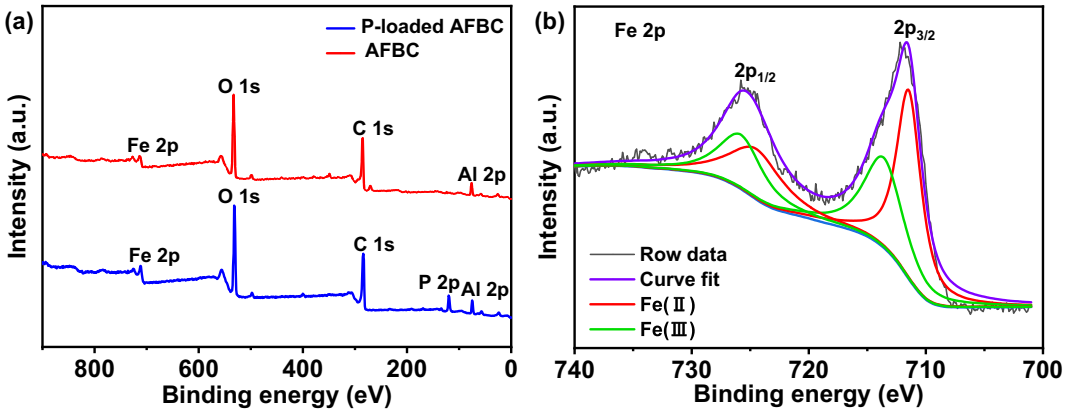

Fig. 2. XPS wide spectra of AFBC before and after phosphate adsorption (a) and Fe 2p (b) spectra of AFBC before phosphate adsorption.

is suggested that the core-shell structure AFBC adsorbent material is synthesized.

3.2. Phosphate adsorption

3.2.1. Effect of solution pH on adsorption

Fig. 3a shows the AFBC phosphate adsorption capacities and the final solution pH (the pH of the solution after reaching the adsorption equilibrium) within a pH range of 3.0–11.0. These results confirm that phosphate adsorption onto AFBC was highly dependent upon pH. The amount of adsorbed phosphate increased gradually from 28.4 to 35.1 mg g^{-1} as the pH increased from 3.0 to 5.0, and then decreased to 12.6 mg g^{-1} as the pH increased from 5.0 to 11.0. The AFBC adsorption capacity increased with an increase in pH because a low pH (3.0–4.0) destroyed the AFBC surface spinel structure. Therefore, an optimal pH value of 5 was selected. To further understand the influence of pH on phosphate adsorption, the point of zero charge (pH_{pzc}) of AFBC was measured at different pH values. The pH_{pzc} of AFBC was 6.8 (Fig. 3b). Among the four phosphate forms (H_3PO_4, $H_2PO_4^-$, HPO_4^{2-}, and PO_4^{3-}; Fig. S4), $H_2PO_4^-$ was the dominant species within the pH range of 3.0–6.0 (Fu et al., 2018). Within this range, the Al oxides would be protonated into $\equiv AlOH_2^+$. Therefore, it is possible that the existing $\equiv AlOH_2^+$ groups will act as active sites for $H_2PO_4^-$ adsorption through electrostatic interaction (Peng et al., 2019). Conversely, at pH levels above 7.0, the concentration of OH^- effectively competed for adsorption sites with PO_4^{3-} in solution, resulting in a decreased capacity for phosphate adsorption (Wu et al., 2019; Wu et al., 2017). When pH levels increased to 11.0, the AFBC adsorption capacity decreased sharply, which was also likely to be related to the destruction of the AFBC surface spinel structure. The pH_{pzc} decreased to 5.1 following phosphate adsorption, which further confirmed the decrease in the positive charge on the AFBC surface after adsorption of phosphate radicals. Overall, these results confirmed that phosphate could be adsorbed onto the AFBC via electrostatic attraction.

Table S4 summarized the ion leaching experiment of FBC and AFBC in solution. The Fe^{2+}/Fe^{3+} dissolution concentration of FBC and AFBC after P adsorption were 93.26 and 0.81 ppb respectively when the pH level was 5.0. This indicates that the γ-Al_2O_3 shell has a good protective effect on Fe_3O_4. When comparing the Al^{3+} dissolution data of AFBC (pH = 5.0 and 11.0), it can be concluded that the dissolution concentration of Al^{3+} was very small (almost negligible) when the pH was 5.0, When the pH was 10.0, the concentration of Al^{3+} was low, indicating that the spinel structure of γ-Al_2O_3 remains stable at that pH. Thus, the spinel structure of γ-Al_2O_3 is well preserved in both weakly acidic and weakly basic solutions.

3.2.2. Adsorption kinetics

The kinetics of phosphate adsorption onto AFBC are presented in Fig. 4a. In the initial reaction stage, AFBC adsorbed phosphate at an exponential rate within the first 2 h, reaching 32.9 mg g^{-1}. Subsequently, the adsorption rate decreased with time, reaching the adsorption equilibrium stage at ~6 h, with the adsorption capacity reaching 35.1 mg g^{-1}. The initial rapid adsorption may be due to electrostatic attraction, leading to rapid migration of phosphate from the solution to the AFBC surface (Cui et al., 2019). The subsequent slow adsorption process showed that as more phosphate ions migrated to the AFBC surface, the surface's positive charge gradually decreased and, at that point, spherical complexation became the main mechanism for phosphate adsorption (Jung et al., 2017b). The pseudo-first-order and pseudo-second-order kinetic models were used to fit the phosphate adsorption kinetics onto AFBC (Ho and McKay, 1998; Lagergren, 1898). Table S1 outlines the detailed description regarding these models and Table 2 summarizes the corresponding kinetic parameters. The predicted q_e value of the pseudo-second-order model (35.8 mg g^{-1}) showed a stronger agreement with the experimental q_e value (35.1 mg g^{-1}) than pseudo-first-order models with higher correlation coefficients (R^2). The pseudo-second-order model ($R^2 = 0.990$) simulated the phosphate adsorption process better than the pseudo-first-order model ($R^2 = 0.985$), suggesting that phosphate adsorption on AFBC was primarily controlled via chemisorption. The representation of experimental data by the intraparticle diffusion model demonstrates three linear segments (Fig. S5), indicating that the adsorption process can be described by film diffusion followed by particle diffusion, an reported by He et al. (2017) and Yang et al. (2019b). At the beginning of adsorption, pHosphate ions were adsorbed onto the exterior surface of AFBC. As the external surface of the adsorbent reached saturation, phosphate ions were further sequestrated into the interior surface of the AFBC in the intraparticle diffusion process. With phosphate concentrations increasing on the interior surface, the diffusion resistance increased, thereby causing the intraparticle diffusion rate to decrease (Peng et al., 2019; Yang et al., 2019b). As shown in Table 2, the value of k_{i1} was larger than k_{i2}, indicating that intraparticle diffusion was the rate-controlling process (He et al., 2017).

3.2.3. Adsorption isotherms

To evaluate the adsorption capacity of phosphate onto AFBC, the adsorption isotherms are presented in Fig. 4b. As discussed above, increasing the initial P concentration gradually increased the AFBC adsorption capacity. Table S1 outlines the data derived from the Langmuir, Freundlich, and Langmuir-Freundlich isotherm models for phosphate adsorption, while Table 2 lists the related parameter fitting from the three models. Correlation coefficients (R^2) of the three models were 0.977, 0.872, and 0.997, respectively, which indicates that Langmuir-

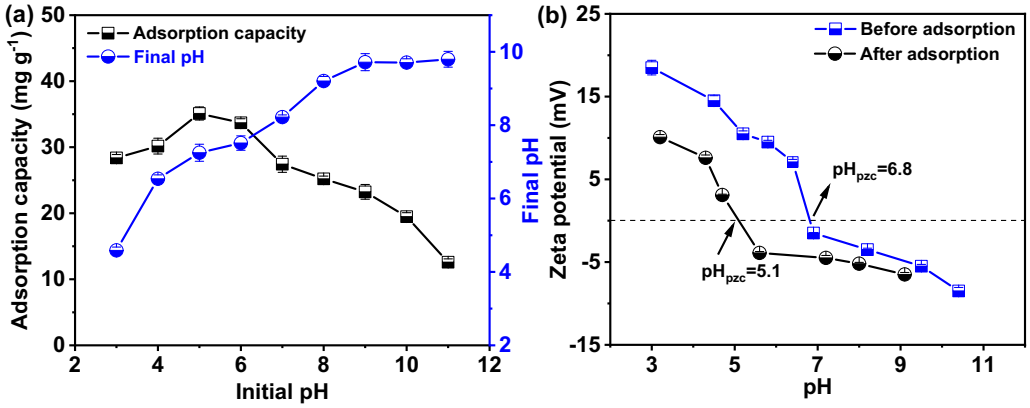

Fig. 3. (a) Effect of initial pH on phosphate adsorption capacities of AFBC and final pH (the pH of the solution after adsorption equilibrium) variation of solution and (b) zeta potential of the AFBC before and after phosphate adsorption at different pH values (sorbent dose = 0.05 g; initial P concentration = 50 mg L^{-1}).

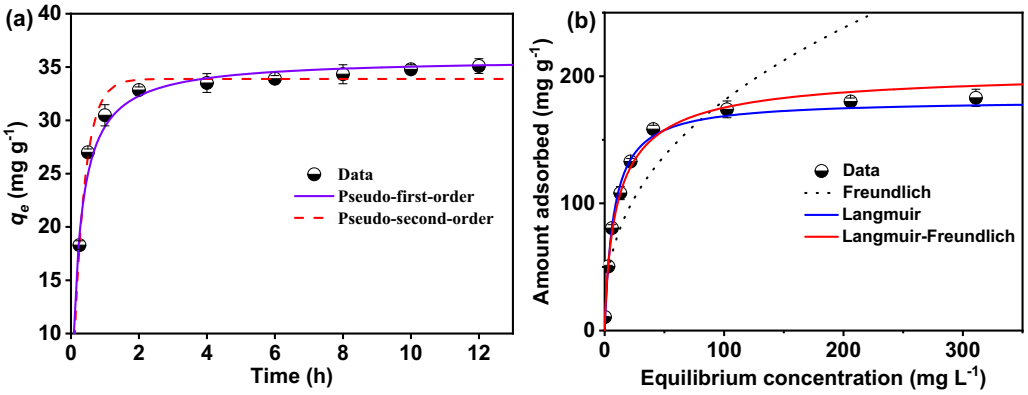

Fig. 4. Phosphate adsorption on AFBC: (a) kinetics and (b) isotherms (sorbent dose = 0.05 g; initial P concentration of kinetics = 50 mg L^{-1}; initial P concentration range of isotherm = 5–500 mg L^{-1}; solution volume = 50 mL; pH 5.0 ± 0.1).

Freundlich more accurately predicted adsorption. This result is consistent with our kinetic studies and indicates that phosphate adsorption onto AFBC is controlled by multiple processes: (i) electrostatic attraction of AFBC to P-containing anion acid roots in solution, and (ii) inner-sphere complexation (Pinto et al., 2019; Yao et al., 2011). The maximum theoretical adsorption capacity (q_m) of AFBC at 25 °C, calculated by the Langmuir-Freundlich isothermal equation, was 205.7 mg g^{-1} which far exceeds the adsorption capacity of magnetic metal (iron)-modified biochar reported by Yang et al. (2018). Compared to previously described iron modified magnetic biochar, further modification of the magnetic biochar Fe_3O_4 by γ-Al_2O_3 with a high specific surface area significantly increased the P adsorption capacity of the modified biochar. It is not objective to do such judgement about the performance of the adsorbent based on adsorption capacity alone because the maximum adsorption capacity is sensitively affected by the initial loading concentration of target pollutants (Younis et al., 2020). The partition coefficient (PC) for a solid-liquid adsorption system represents the ratio of the concentration of adsorbate in the solid adsorbent phase to that in the liquid phase at equilibrium, which can better indicate the performance of the adsorbent (Al-Wabel et al., 2019; O'Connor and Connolly, 1980; Vikrant and Kim, 2018). Therefore, we evaluated the adsorption performance of AFBC (Table S5) and compared it with the performance of other adsorbent materials reported (Table 3). The PC values decreased with an increase in the initial concentration (Table S5), and when the initial concentration was 3.2E+02 μM, the PC value was 1.04 mg g^{-1} μM^{-1}. However, an increase in the initial concentration to 1.6E+04 μM resulted in a PC of only 1.8E-02 mg g^{-1} μM^{-1}. Although the adsorption amount of AFBC can be up to 183.01 mg g^{-1} at the initial concentration 1.6E+04 μM, the PC is only 1.8E-02 mg g^{-1} μM^{-1}, indicating that a large amount of phosphate remained in solution. At a low initial concentration of 1.6E+03 μM, the adsorption capacity is 43.9 mg g^{-1}, and the PC value is up to 2.2E-01 mg g^{-1} μM^{-1}, indicating that AFBC has a great removal effect at low P concentrations. The above PC results confirmed that AFBC is more suitable for low-concentration P removal than high-concentration, supported by Jack et al. (2019) and Xiong et al. (2017). Different absorbents reported were effective in the removal of phosphate (Table 3). In comparison with previous studies, AFBC exhibits excellent adsorption performance at lower phosphate concentration. Furthermore, when developing an adsorbent material for application in the field, other aspects must be considered. The biochar modified in this study is more advantageous in terms of the availability of the material source and it has a high-value recycling use of biomass wastes.

3.2.4. Effect of coexisting anions

The interference in AFBC phosphate adsorption performance from naturally coexisting substances (including SO_4^{2-}, Cl^-, HCO_3^-, NO_3^-, F^-, and a mixture of these anions) was investigated, and the results are summarized in Fig. S6. Despite increasingly higher concentrations of SO_4^{2-}, Cl^-, HCO_3^-, and NO_3^-, AFBC phosphate adsorption capacity incurred only minor losses (1.7%–7.4%), even when the concentrations of theses ions reached 1.0 mmol L^{-1}. These results suggest that the high selectivity of AFBC for phosphate capture was largely unaffected by varying the concentrations of coexisting ions; this can be attributed to the strong and stable interactions between AFBC and most phosphate anions, and the formation of inner-sphere complexes with metal oxides (Kong et al., 2019). In contrast, F^- and anion mixture caused up to 15.9% and 18.5% decreases in phosphate adsorption capacity, respectively. F^- has a strong electro-negativity and can be easily combined with the protonated adsorbent surface (Kumar et al., 2011). In contrast, the F^- removal process has been shown to involve the replacement of OH^- with F^- (Hu et al., 2005). Zhang et al. (2002) studied the interaction of F^- on γ-Al_2O_3 surface by multinuclear MAS NMR spectroscopy to identify the fluorine species on the fluorinated γ-Al_2O_3. The spectroscopic analysis indicated that F^- enters the surface of alumina by substituting hydroxyl groups without breaking the bridging Al–O–Al

Table 2
Best-fit parameter values from model simulations of phosphate adsorption kinetics and isotherms about AFBC.

	Parameter 1	Parameter 2	Parameter 3	R^2
Adsorption kinetics				
Experimental results		q_e = 35.1 (mg g^{-1})		
Pseudo-first-order	k_1 = 3.072 (1 h^{-1})	q_e = 33.9 (mg g^{-1})		0.985
Pseudo-second-order	k_2 = 0.129 (g mg^{-1} h^{-1})	q_e = 35.8 (mg g^{-1})		0.990
Intraparticle diffusion	k_{i1} = 45.412 (mg g^{-1}·$h^{1/2}$)	C_1 = −4.937 (mg g^{-1})		R^2 (k_{i1}) = 0.998
	k_{i2} = 8.232 (mg g^{-1}·$h^{1/2}$)	C_2 = 21.242 (mg g^{-1})		R^2 (k_{i2}) = 0.988
	k_{i3} = 1.088 (mg g^{-1}·$h^{1/2}$)	C_3 = 31.291 (mg g^{-1})		R^2 (k_{i3}) = 0.996
Adsorption isotherms				
Langmuir	K_L = 0.132 (L mg^{-1})	Q_m = 181.4 (mg g^{-1})		0.977
Freundlich	K_F = 29.160 (mg g^{-1})	n = 2.525		0.872
Langmuir-Freundlich	K_{LF} = 0.137 (L mg^{-1})	Q_m = 205.7 (mg g^{-1})	n = 1.232	0.997

Table 3
Performance comparison of different adsorbents tested for phosphate removal.

Sorbents	Sorption conditions	Initial concentration	Equilibrium concentration	Adsorption capacity	PC (100% BT)	Ref.
	°C, pH	μM	μM	mg g^{-1}	mg g^{-1} μM^{-1}	
Magnetic water hyacinth biochar	25, 7.0	4.8E+03	4.7E+03	5.07	1.1E−03	Cai et al., 2017
Iron-zirconium/activated carbon nanofiber	25, 4.0	3.2E+02	2.4E+02	26.3	1.1E−01	Xiong et al., 2017
Magnetic fungal biomass biochar	25, NR	2.9E+03	1.4E+03	23.9	7.2E−04	Jack et al., 2019
$MgFe_2O_4$/biochar magnetic composites	20, 3.0	5.3E+03	4.2E+03	159.2	2.4E−04	Jung et al., 2017b
$La(OH)_3$-modified magnetic biochar	30, NR	1.3E+04	9.6E+03	101.2	1.1E−02	Liao et al., 2018
Ferrihydrite/lanthanum-decorated magnetite	25, 6.3	1.1E+03	2.7E+02	44.8	1.7E−01	Fu et al., 2018
AFBC	25, 5.0	1.6E+04	1.0E+04	183.01	1.8E−02	This study

Note: PC: Partition coefficient; NR: no report.

bonds. At higher F^- loadings, bridging Al–O–Al bonds were found to be broken to adsorb more F^- under the strong electron-withdrawing effect of fluorine. Therefore, the adsorption of phosphate significantly decreased with the coexistence of F^-.

3.3. Mechanism of adsorption

To further explore the adsorption mechanism of phosphate on the AFBC adsorbent, the chemical states and composition of AFBC before and after phosphate adsorption were analyzed by XPS. Fig. 5 shows the O 1 s, Al 2p, and Fe 2p XPS spectra. The O 1 s spectra of AFBC was also examined to investigate the interaction of phosphate with the AFBC. According to the binding energy of different oxygen species on AFBC, the XPS spectra of O 1 s exhibited two peaks (Al—O and Al–OH) at 530.4 and 531.8 eV. After phosphate uptake, the XPS spectra of O 1 s added a P—O peak at 531.5 eV. The relative proportions of each oxygen species were calculated and are presented in Fig. 5a. Compared with phosphate uptake, the percentage of P—O increased from 0% to 6.1% and the percentage of Al—O increased from 38.5% to 41.2%, while the percentage of Al–OH decreased from 61.5% to 52.7%. The decreased Al–OH ratio suggests that hydroxyl groups on the surface of aluminum oxide play an important role in phosphate adsorption. Phosphate adsorption by AFBC was largely due to the inner-sphere complexation that occurred via ligand exchange reactions with surface hydroxyl groups replaced by phosphate ions (Blaney et al., 2007; Peng et al., 2019). In previous studies, a similar mechanism was also reported regarding anion adsorption on iron oxide and titanium oxide (Nie et al., 2019; Jack et al., 2019). Fig. 5b displays the Al 2p XPS spectra of AFBC. The Al 2p binding energy decreased from 75.6 to 74.9 eV, while the Fe $2p_{3/2}$ spectra (Fig. 5c) showed a small change (from 711.2 to 711.3 eV). These changes indicate that Al hydroxides and Fe_3O_4 participated in the P adsorption process. However, Fe_3O_4 was less dominant compared to γ-Al_2O_3 during the P adsorption process, likely due to protection effect of γ-Al_2O_3 on Fe_3O_4.

Regarding inner-sphere complexation, the possible inner-sphere phosphate complexes can be postulated to form monodentate

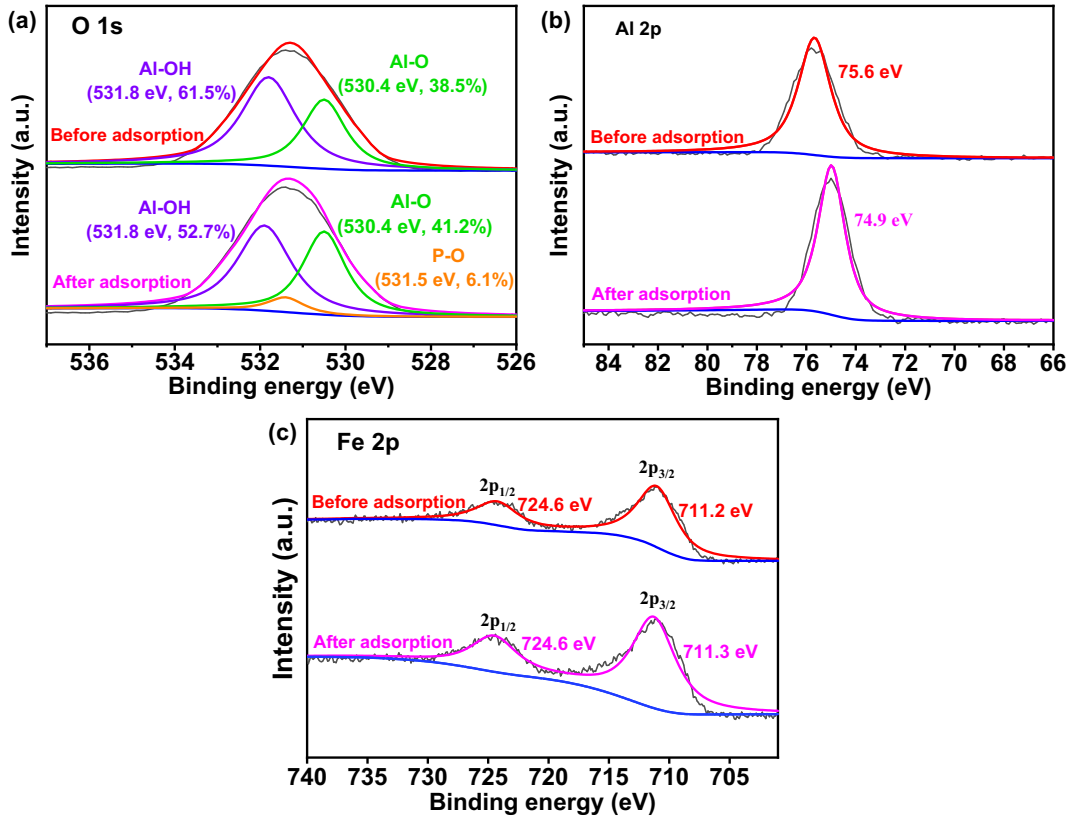

Fig. 5. The XPS analysis of the O 1s (a), Al 2p (b) and Fe 2p (c) before and after phosphate adsorption.

mononuclear and bidentate binuclear species, as shown in reactions (4) and (5), respectively, in the AFBC adsorbent; the formation of these complexes are described as follows (Nero et al., 2010):

$$\equiv AlOH_2^+ + H_2PO_4^- \leftrightarrow \equiv AlOPO_3^{2-} + H_2O + 2H^+ \quad (4)$$

$$2 \equiv AlOH_2^+ + H_2PO_4^- \leftrightarrow \equiv Al_2O_2PO_2^- + 2H_2O + 2H^+ \quad (5)$$

Saifuddin et al. (2019) also reported that aluminum oxide and phosphate at the same pH (5.0) formed monodentate mononuclear and bidentate binuclear species. In accordance with the above discussion, the possible AFBC phosphate adsorption mechanisms are summarized in Fig. 6.

3.4. AFBC reusability and P recovery

In addition to exclusive or highly selective adsorption, reusability of a composite adsorbent is another required feature for its practical use. Consistent with the notion that high pH conditions lead to poor phosphate adsorption, as observed in our pH study, adsorbed phosphate can be eluted from the AFBC adsorbent by inducing alkaline conditions ($pH > pH_{pzc}$). Therefore, we performed phosphate desorption from phosphate-loaded AFBC at different NaOH concentrations ranging from 1.0×10^{-6} to 1.0×10^{-2} mol L^{-1} (Fig. S7). The desorption efficiency of phosphate was calculated as the ratio of desorbed phosphate to adsorbed phosphate (Eq. (3)). With increasing NaOH concentrations the desorption efficiency gradually increased from 17.3% to 96.2%. However, AFBC may decompose when the NaOH concentration reaches 1.0×10^{-3}–1.0×10^{-2} mol L^{-1}, despite a high P removal rate. Hence, an optimal condition of 1.0×10^{-4} mol L^{-1} NaOH was selected for the P recovery process at 81.7% desorption efficiency. Fig. 7 shows no significant difference in the removal efficiency at the beginning of 5 cycles, but significant differences are observed after 5 cycles ($P < .05$). Removal efficiency remained high at approximately 91.0% after 5 cycles. This phenomenon could be due to the depletion of available active adsorption sites. The difference in desorption efficiency was not significant in the first 6 cycles, but was significant in the seventh cycle ($P < .05$). After 6 cycles, the desorption efficiency remained above 91.3%.

Reusability test results demonstrated that AFBC collection is convenient and has excellent adsorption and desorption efficiency after multiple reuse, highlighting the practicality and stability of AFBC in P recovery. Subsequently, the desorbed P-rich solution can be used to produce phosphate fertilizer and achieve the purpose of P recovery and reuse.

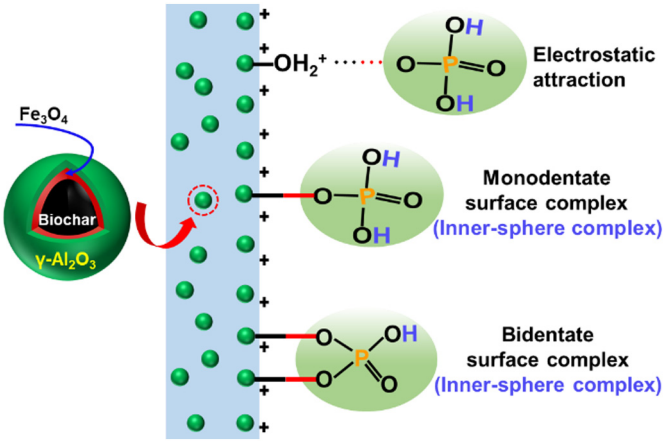

Fig. 6. Mechanism of AFBC for phosphate adsorption.

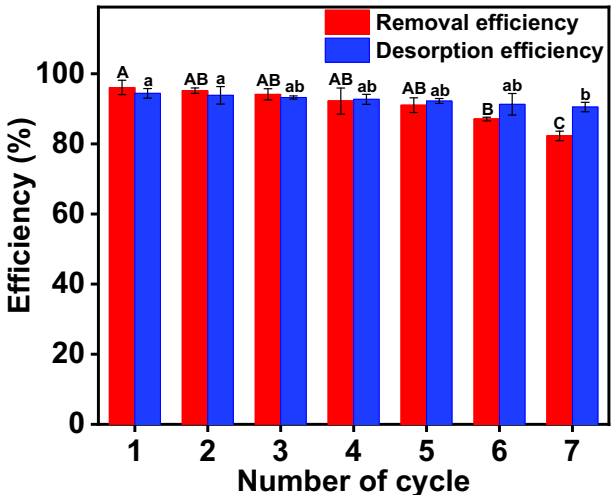

Fig. 7. Adsorption and desorption efficiency of AFBC in seven adsorption-desorption cycles. Different uppercase letters (A, B, and C) indicate that means are significantly different ($P < .05$) among different P removal cycles; whereas different lowercase letters (a and b) indicate that means are significantly different ($P < .05$) among different P desorption cycles. (sorbent dose = 0.05 g; initial P concentration = 35 mg L^{-1}; solution volume = 50 mL; pH 5.0 ± 0.1).

4. Conclusions

Synthesized biochar-based core-shell complex AFBC is an anionic adsorbent possessing many excellent properties: high P adsorption capacity (205.7 mg g^{-1}), convenient recyclability, and stable reusability (91.0% removal efficiency after five adsorption-desorption cycles and 91.3% desorption efficiency after six adsorption-desorption cycles). Electrostatic attraction and inner-sphere complexation were found to be the common mechanisms of P adsorption onto AFBC. The inner-sphere phosphate complex comprised $\equiv AlOPO_3^{2-}$ and $\equiv Al_2O_2PO_2^-$ in the AFBC adsorbent. Moreover, AFBC exhibited excellent uptake performance even in the presence of large excesses of other competing anions. This study provides a new method for synthesizing biochar core-shell composite materials that effectively avoids secondary pollution as well as mechanistic insights into the interaction between phosphate and biochar-based adsorbents.

Acknowledgements

This work was supported by the National Natural Science Foundation of China (41571225), the National Key Research and Development of China (2016YFC0501702, 2017YFC0504504), and Science and Technology Service Network Initiative of the Chinese Academy of Sciences (KFJ-STS-QYZD-177). We also thank the instrument analysis center of Xi'an Jiaotong University (XJTU, China).

Appendix A. Supplementary data

Supplementary data to this article can be found online at https://doi.org/10.1016/j.scitotenv.2020.138892.

References

Al-Wabel, M., Elfaki, J., Usman, A., Hussain, Q., OK, Y.S., 2019. Performance of dry water- and porous carbon-based sorbents for carbon dioxide capture. Environ. Res. 174, 69–79.

Blaney, L.M., Cinar, S., SenGupta, A.K., 2007. Hybrid anion exchanger for trace phosphate removal from water and wastewater. Water Res. 41, 1603–1613.

Cai, R., Wang, X., Ji, X., Peng, B., Tan, C., Huang, X., 2017. Phosphate reclaim from simulated and real eutrophic water by magnetic biochar derived from water hyacinth. J. Environ. Manag. 187, 212–219.

Chen, B., Chen, Z., Lv, S., 2011. A novel magnetic biochar efficiently sorbs organic pollutants and phosphate. Bioresour. Technol. 102, 716–723.

Cui, Q., Jiao, G., Zheng, J., Wang, T., Wu, G., Li, G., 2019. Synthesis of a novel magnetic *Caragana korshinskii* biochar/mg–Al layered double hydroxide composite and its strong adsorption of phosphate in aqueous solutions. RSC Adv. 9, 18641–18651.

Du, Q., Li, G., Zhang, S., Song, J., Zhao, Y., Yang, F., 2020. High-dispersion zero-valent iron particles stabilized by artificial humic acid for lead ion removal. J. Hazard. Mater. 383, 121170.

Fu, H., Yang, Y., Zhu, R., Liu, J., Usman, M., Chen, Q., He, H., 2018. Superior adsorption of phosphate by ferrihydrite-coated and lanthanum-decorated magnetite. J. Colloid Interface Sci. 530, 704–713.

Han, M., Zhang, J., Hu, Y., Han, R., 2019. Preparation of novel magnetic microspheres with the La and Ce-bimetal oxide shell for excellent adsorption of fluoride and phosphate from solution. J. Chem. Eng. Data 64, 3641–3651.

He, Y., Lin, H., Dong, Y., Wang, L., 2017. Preferable adsorption of phosphate using lanthanum-incorporated porous zeolite: characteristics and mechanism. Appl. Surf. Sci. 426, 995–1004.

Ho, Y.S., McKay, G., 1998. Sorption of dye from aqueous solution by peat. Chem. Eng. J. 70, 115–124.

Hu, C.Y., Lo, S.L., Kuan, W.H., 2005. Effects of the molar ratio of hydroxide and fluoride to Al(III) on fluoride removal by coagulation and electrocoagulation. J. Colloid Interface Sci. 283, 472–476.

Huang, H., Yang, J., Li, D., 2014. Recovery and removal of ammonia-nitrogen and phosphate from swine wastewater by internal recycling of struvite chlorination product. Bioresour. Technol. 172, 253–259.

Jack, J., Huggins, T.M., Huang, Y., Fang, Y., Ren, Z.J., 2019. Production of magnetic biochar from waste-derived fungal biomass for phosphorus removal and recovery. J. Clean. Prod. 224, 100–106.

Jung, K., Choi, B.H., Ahn, K., Lee, S., 2017a. Synthesis of a novel magnetic Fe_3O_4/γ-Al_2O_3 hybrid composite using electrode-alternation technique for the removal of an azo dye. Appl. Surf. Sci. 423, 383–393.

Jung, K., Lee, S., Lee, Y., 2017b. Synthesis of novel magnesium ferrite ($MgFe_2O_4$)/biochar magnetic composites and its adsorption behavior for phosphate in aqueous solutions. Bioresour. Technol. 245, 751–759.

Jung, K.W., Hwang, M.J., Jeong, T.U., Ahn, K.H., 2015. A novel approach for preparation of modified-biochar derived from marine macroalgae: dual purpose electro-modification for improvement of surface area and metal impregnation. Bioresour. Technol. 191, 342–345.

Jung, Y., Ko, Y.G., Do, T., Chun, Y., Choi, U.S., Kim, C.H., 2019. Core/shell hybrid fiber with aminated PAN and Fe_2O_3 as a high-capacity adsorbent for phosphate ions. J. Hazard. Mater. 378, 120726.

Kong, L., Han, M., Shih, K., Su, M., Diao, Z., Long, J., Chen, D., Hou, L., Peng, Y., 2018. Nano-rod Ca-decorated sludge derived carbon for removal of phosphorus. Environ. Pollut. 233, 698–705.

Kong, L., Tian, Y., Pang, Z., Huang, X., Li, Ming, Yang, R., Li, N., Zhang, J., Zuo, W., 2019. Synchronous phosphate and fluoride removal from water by 3D rice-like lanthanum-doped La@MgAl nanocomposites. Chem. Eng. J. 371, 893–902.

Kumar, E., Bhatnagar, A., Kumar, U., Sillanpää, M., 2011. Defluoridation from aqueous solutions by nano-alumina: characterization and sorption studies. J. Hazard. Mater. 186, 1042–1049.

Lagergren, S., 1898. About the theory of so-called adsorption of soluble substances. K. Sven. Veten. Hand. 24, 1–39.

Lan, S., Guo, N., Liu, L., Wu, X., Li, L., Gan, S., 2013. Facile preparation of hierarchical hollow structure gamma alumina and a study of its adsorption capacity. Appl. Surf. Sci. 283, 1032–1040.

Leng, L., Yuan, X., Zeng, G., Shao, J., Chen, X., Wu, Z., Wang, H., Peng, X., 2015. Surface characterization of rice husk biochar produced by liquefaction and application for cationic dye (malachite green) adsorption. Fuel 155, 77–85.

Li, R., Wang, J.J., Zhou, B., Awasthi, M.K., Ali, A., Zhang, Z., Gaston, L.A., Lahori, A.H., Mahar, A., 2016. Enhancing phosphate adsorption by mg/Al layered double hydroxide functionalized biochar with different mg/Al ratios. Sci. Total Environ. 559, 121–129.

Li, R., Wang, J.J., Zhang, Z., Awasthi, M.K., Du, D., Dang, P., Huang, Q., Zhang, Y., Wang, L., 2018. Recovery of phosphate and dissolved organic matter from aqueous solution using a novel CaO-MgO hybrid carbon composite and its feasibility in phosphorus recycling. Sci. Total Environ. 642, 526–536.

Li, X., Zhao, R., Sun, B., Lu, X., Zhang, C., Wang, Z., Wang, C., 2014. Fabrication of alpha-Fe_2O_3-gamma-Al_2O_3 core-shell nanofibers and their Cr(VI) adsorptive properties. RSC Adv. 4, 42376–42382.

Liao, T., Li, T., Su, X., Yu, X., Song, H., Zhu, Y., Zhang, Y., 2018. $La(OH)_3$-modified magnetic pineapple biochar as novel adsorbents for efficient phosphate removal. Bioresour. Technol. 263, 207–213.

Liu, W., Jiang, H., Yu, H., 2015. Development of biochar-based functional materials: toward a sustainable platform carbon material. Chem. Rev. 115, 12251–12285.

Lǚ, J., Liu, H., Liu, R., Zhao, X., Sun, L., Qu, J., 2013. Adsorptive removal of phosphate by a nanostructured Fe-Al-Mn trimetal oxide adsorbent. Powder Technol. 233, 146–154.

Lu, X., Yu, Y., Chen, L., Mao, H., Gao, H., Wang, J., Yen, W., 2005. Aniline dimer-COOH assisted preparation of well-dispersed polyaniline-Fe_3O_4 nanoparticles. Nanotechnology 16, 1660–1665.

Mayer, B.K., Baker, L.A., Boyer, T.H., Drechsel, P., Gifford, M., Hanjra, M.A., Parameswaran, P., Stoltzfus, J., Westerhoff, P., Rittmann, B.E., 2016. Total value of phosphorus recovery. Environ. Sci. Technol. 50, 6606–6620.

Murphy, J., Riley, J.P., 1962. A modified single solution method for the determination of phosphate in natural waters. Anal. Chim. Acta 27, 31–36.

Nero, M.D., Galindo, C., Barillon, R., Halter, E., Madé, B., 2010. Surface reactivity of α-Al_2O_3 and mechanisms of phosphate sorption: *In situ* ATR-FTIR spectroscopy and ζ potential studies. J. Colloid Interf. Sci. 342, 437–444.

Nie, G., Wu, L., Du, Y., Wang, H., Xu, Y., Ding, Z., Liu, Z., 2019. Efficient removal of phosphate by a millimeter-sized nanocomposite of titanium oxides encapsulated in positively charged polymer. Chem. Eng. J. 360, 1128–1136.

O'Connor, D.J., Connolly, J.P., 1980. The effect of concentration of adsorbing solids on the partition coefficient. Water Res. 14, 1517–1523.

Peng, Y., Sun, Y., Sun, R., Zhou, Y., Tsang, D.C., Chen, Q., 2019. Optimizing the synthesis of Fe/Al (Hydr)oxides-biochars to maximize phosphate removal via response surface model. J. Clean. Prod. 237, 117770.

Pinto, M.C.E., Silva, D.D., Gomes, A.L.A., Santos, R.M.M., Couto, R.A.A., Novais, R.F., Constantino, V.R.L., Tronto, J., Pinto, F.G., 2019. Biochar from carrot residues chemically modified with magnesium for removing phosphorus from aqueous solution. J. Clean. Prod. 222, 36–46.

Saifuddin, M., Bae, J., Kim, K.S., 2019. Role of Fe, Na and Al in Fe-zeolite-a for adsorption and desorption of phosphate from aqueous solution. Water Res. 158, 246–256.

Salama, A., 2018. Chitosan based hydrogel assisted spongelike calcium phosphate mineralization for in-vitro BSA release. Int. J. Biol. Macromol. 108, 471–476.

Schmale, D.G., Ault, A.P., Saad, W., Scott, D.T., Westrick, J.A., 2019. Perspectives on harmful algal blooms (HABs) and the cyberbiosecurity of freshwater systems. Front. Bioeng. Biotech. 7, 128.

Shanmugam, S., Nakanishi, T., Osaka, T., 2009. Morphology and magnetic properties of iron oxide nanostructures synthesized with biogenic polyamines. J. Electrochem. Soc. 156, K121–K127.

Shemer, H., Armush, A., Semiat, R., 2019. Reusability of iron oxyhydroxide agglomerates adsorbent for repetitive phosphate removal. Colloids Surf. A Physicochem. Eng. Asp. 579, 123680.

Tang, J., Zhu, N., Zhu, Y., Liu, J., Wu, C., Kerr, P., Wu, Y., Lam, P., 2017. Responses of periphyton to Fe_2O_3 nanoparticles: a physiological and ecological basis for defending nanotoxicity. Environ. Sci. Technol. 51, 10797–10805.

Tonini, D., Saveyn, H.G.M., Huygens, D., 2019. Environmental and health co-benefits for advanced phosphorus recovery. Nat. Sustain. 2, 1051–1061.

Vikrant, K., Kim, K.-H., 2018. Nanomaterials for the adsorptive treatment of hg (II) ions from water. Chem. Eng. J. 358, 264–282.

Vilmin, L., Mogollón, J.M., Beusen, A.H.W., Bouwman, A.F., 2018. Forms and subannual variability of nitrogen and phosphorus loading to global river networks over the 20th century. Glob. Planet. Chang. 163, 67–85.

Wang, L., Wang, J., He, C., Lyu, W., Zhang, W., Yan, W., Yang, L., 2019. Development of rare earth element doped magnetic biochars with enhanced phosphate adsorption performance. Colloids Surf. A Physicochem. Eng. Asp. 561, 236–243.

Wang, S., Kong, L., Long, J., Su, M., Diao, Z., Chang, X., Chen, D., Song, G., Shih, K., 2018. Adsorption of Phosphorus by Calcium-Flour Biochar: Isotherm, Kinetic and Transformation Studies. 195 pp. 666–672.

Wu, B., Fang, L., Fortner, J.D., Guan, X., Lo, I.M.C., 2017. Highly efficient and selective phosphate removal from wastewater by magnetically recoverable $La(OH)_3$/Fe_3O_4 nanocomposites. Water Res. 126, 179–188.

Wu, L., Wei, C., Zhang, S., Wang, Y., Kuzyakov, Y., Ding, X., 2019. MgO-modified biochar increases phosphate retention and rice yields in saline-alkaline soil. J. Clean. Prod. 235, 901–909.

Wu, Y., Liu, J., Yang, L., Chen, H., Zhang, S., Zhao, H., Zhang, N., 2011. Allelopathic control of cyanobacterial blooms by periphyton biofilms. Environ. Microbiol. 13, 604–615.

Xiao, X., Chen, B., Chen, Z., Zhu, L., Schnoor, J.L., 2018. Insight into multiple and multilevel structures of biochars and their potential environmental applications: a critical review. Environ. Sci. Technol. 52, 5027–5047.

Xiong, W., Tong, J., Yang, Z., Zeng, G., Zhou, Y., Wang, D., Song, P., Xu, R., Zhang, C., Cheng, C., 2017. Adsorption of phosphate from aqueous solution using iron-zirconium modified activated carbon nanofiber: performance and mechanism. J. Colloid Interface Sci. 493, 17–23.

Xu, J., Koopal, L.K., Wang, M., Xiong, J., Hou, J., Li, Y., Tan, W., 2019. Phosphate speciation on Al-substituted goethite: ATR-FTIR/2D-COS and CD-MUSIC modeling. Environ. Sci.: Nano. 6, 3625–3637.

Yan, J., Jiang, T., Yao, Y., Lu, S., Wang, Q., Wei, S., 2016. Preliminary investigation of phosphorus adsorption onto two types of iron oxide-organic matter complexes. J. Environ. Sci. 42, 152–162.

Yan, L., Yang, K., Shan, R., Yan, T., Wei, J., Yu, S., Y, H., Du, B., 2015. Kinetic, isotherm and thermodynamic investigations of phosphate adsorption onto core-shell Fe_3O_4@LDHs composites with easy magnetic separation assistance. J. Colloid Interf. Sci. 448, 508–516.

Yang, F., Zhang, S., Sun, Y., Du, Q., Song, J., Tsang, D.C.W., 2019a. A novel electrochemical modification combined with one-step pyrolysis for preparation of sustainable thorn-like iron-based biochar composites. Bioresour. Technol. 274, 379–385.

Yang, F., Zhang, S., Sun, Y., Tsang, D.C.W., Cheng, K., Ok, Y.S., 2019b. Assembling biochar with various layered double hydroxides for enhancement of phosphorus recovery. J. Hazard. Mater. 365, 665–673.

Yang, F., Zhang, S., Cho, D., Du, Q., Song, J., Tsang, D.C.W., 2019c. Porous biochar composite assembled with ternary needle-like ironmanganese-Sulphur hybrids for high-efficiency lead removal. Bioresour. Technol. 272, 415–420.

Yang, Q., Wang, X., Luo, W., Sun, J., Xu, Q., Chen, F., Zhao, J., Wang, S., Yao, F., Wang, D., Li, X., Zeng, G., 2018. Effectiveness and mechanisms of phosphate adsorption on iron-modified biochars derived from waste activated sludge. Bioresour. Technol. 247, 537–544.

Yao, Y., Gao, B., Inyang, M., Zimmerman, A.R., Cao, X., Pullammanappallil, P., Yang, L., 2011. Removal of phosphate from aqueous solution by biochar derived from anaerobically digested sugar beet tailings. J. Hazard. Mater. 190, 501–507.

Yi, M., Chen, Y., 2018. Enhanced phosphate adsorption on Ca-mg-loaded biochar derived from tobacco stems. Water Sci. Technol. 78, 2427–2436.

Younis, S.A., El-Salamony, R.A., Tsang, Y.F., Kim, K., 2020. Use of rice straw-based biochar for batch sorption of barium/ strontium from saline water: protection against scale formation in petroleum/desalination industries. J. Clean. Prod. 250, 119442.

Zhang, W., Sun, M., Prins, R., 2002. Multinuclear MAS NMR identification of fluorine species on the surface of fluorinated γ-alumina. J. Phys. Chem. B 106, 11805–11809.

Zhu, L., Tong, L., Zhao, N., Li, J., Lv, Y., 2019. Coupling interaction between porous biochar and nano zero valent iron/nano α-hydroxyl iron oxide improves the remediation efficiency of cadmium in aqueous solution. Chemosphere 219, 493–503.

Zhu, Z., Huang, C., Zhu, Y., Wei, W., Qin, H., 2018. A hierarchical porous adsorbent of nano-α-Fe_2O_3/Fe_3O_4 on bamboo biochar (HPA-Fe/C-B) for the removal of phosphate from water. J. Water Process Eng. 25, 96–104.